ceramics

MDPI

Article

Density Functional Theory Study of Pressure-Dependent Structural and Electronic Properties of Cubic Zirconium Dioxide

Zhussupbek M. Salikhodzha [1], Guldari B. Bairbayeva [1,*], Raigul N. Kassymkhanova [1], Marina Konuhova [2], Keleshek B. Zhangylyssov [1], Elena Popova [3,*] and Anatoli I. Popov [1]

1. Institute of Physical and Technical Sciences, Faculty Transport and Energy, L.N. Gumilyov Eurasian National University, 13 Kazhymukan St., Astana 010000, Kazakhstan; salikhodzha_zhm@enu.kz (Z.M.S.); suleimen_rn@enu.kz (R.N.K.); keleshek92@yandex.ru (K.B.Z.); popov@latnet.lv (A.I.P.)
2. Institute of Solid-State Physics, University of Latvia, LV-1063 Riga, Latvia; mkonuhova@gmail.com
3. Department of Physics, University of Maryland, College Park, MD 20742-4111, USA
* Correspondence: bairbayeva_gb_3@enu.kz (G.B.B.); epopova@umd.edu (E.P.)

Abstract: In this study, the structural, electronic, and elastic properties of cubic zirconium dioxide (c-ZrO_2) were investigated using the Density Functional Theory (DFT) approach. Lattice parameter optimization revealed that the lattice constant is 5.107 Å, the Zr–O bond length is 2.21 Å, and the unit cell density is 6.075 g/cm^3 for the B3LYP functional. The bandgap width was determined to be 5.1722 eV. The investigation of the elastic properties of the cubic ZrO_2 crystal determined the Young's modulus, bulk modulus, Poisson's ratio, and hardness, which were found to be 315.91 GPa, 241 GPa, 0.282, and 13 (Hv), respectively, under zero external pressure. These results confirm the mechanical stability of ZrO_2.

Keywords: first-principles calculation; DFT; structural and electronic properties; elastic properties; cubic zirconia

1. Introduction

Zirconium dioxide (ZrO_2) is a functional material with unique mechanical, thermal, dielectric, and electronic properties [1–7]. Due to these characteristics, it is widely used in industry, including in the production of electrochemical devices, oxygen sensors, photocatalytic systems, and optical instruments [8–12]. Furthermore, the high radiation resistance of ZrO_2 makes it an important material for nuclear technologies, including reactors, inert matrix fuel, radioactive waste disposal systems, and containers for storing radioactive substances [13–18].

At atmospheric pressure, ZrO_2 exists in three crystalline modifications: monoclinic ($P2_1/c$), which is stable at temperatures below 1150 °C, tetragonal ($P4_2/nmc$), existing in the range of 1150–2350 °C, and cubic (Fm3m, fluorite-like structure), which forms at temperatures above 2350 °C [19–23]. The transition between these phases is accompanied by changes in volumetric and mechanical properties, playing a crucial role in adjusting the characteristics of ZrO_2 [24–26]. However, upon cooling, the high-temperature phases of ZrO_2 undergo a martensitic transformation, accompanied by a volume change (~3–5%), which can lead to material cracking. To prevent this effect, ZrO_2 stabilization is carried out by introducing dopants of divalent, trivalent, and tetravalent oxides, such as CaO, MgO, Y_2O_3, La_2O_3, Yb_2O_3, and CeO_2 [27].

Depending on the stabilization conditions, partially stabilized zirconia (PSZ), which contains a mixture of cubic and tetragonal phases and is in demand for mechanical and structural applications, and fully stabilized zirconia (FSZ), which has a purely cubic

structure and is used in oxygen sensors, heating elements, and fuel cells, can be distinguished [24].

ZrO$_2$-based materials possess high strength and resistance to external influences. For example, the electro-consolidation method enables the production of ZrO$_2$ composites with a high reproducibility of mechanical properties due to the precise control of sintering temperature and pressure. It has been established that the stability of elastic characteristics (Young's modulus, hardness) makes such materials promising for aerospace technologies [28].

Additionally, composite materials based on ZrO$_2$, WC, and Al$_2$O$_3$, obtained using lamination and oscillatory pressing methods, exhibit high hardness (30.06 GPa) and fracture toughness (12.04 MPa·m$^1/^2$), which is explained by crack growth inhibition and deflection effects [29].

Besides elastic properties, ZrO$_2$ exhibits interesting electronic characteristics under pressure. Studies by Wu et al. [30] have shown that phase transitions in ZrO$_2$ are accompanied by changes in bandgap width, opening the possibility of tuning its electronic properties. It has been found that at pressures of 17 GPa, the monoclinic phase transitions into the tetragonal phase, and at 44 GPa, this phase transitions into the cubic phase, which is due to dynamic lattice instability.

Hybrid DFT calculations (PBE0) by Eklund et al. [31] have revealed important structural trends confirming the high technological potential of ZrO$_2$. Additionally, it has been established that in the cotunnite phase of ZrO$_2$, high stiffness (bulk modulus of 254 GPa) is realized, which is associated with the dense atomic packing and ninefold coordination of Zr [32].

Despite the widespread use of zirconium dioxide (ZrO$_2$), its behavior under high pressure—particularly regarding the elastic and electronic characteristics of the cubic phase—has not been sufficiently studied. This is especially true for the pressure range of 40–80 GPa, where phase stability, mechanical robustness, and electronic tunability are of considerable technological interest. While previous DFT investigations have largely focused on basic structural properties or bandgap calculations, they often overlook the mechanical response under pressure, including stress–strain behavior, which is challenging to measure experimentally, especially in the low-pressure regime.

In this study, we present a comprehensive first-principles analysis of the structural, elastic, and electronic properties of undoped cubic ZrO$_2$ under hydrostatic pressures up to 80 GPa using the hybrid B3LYP functional. A detailed evaluation of mechanical parameters—such as Young's modulus, Poisson's ratio, bulk modulus, and hardness—is performed, along with an investigation of brittleness and plasticity indicators, allowing us to characterize the material's mechanical performance under extreme conditions.

A key novelty of this work is the application of stress tensor analysis to detect the onset of non-linear mechanical behavior in cubic zirconia. Specifically, we identify a critical deviation from linear elasticity at pressures of approximately 2.4–2.6 GPa, which we interpret as a theoretical yield point—analogous to the transition from elastic to pre-yield regimes commonly observed in mechanical testing. To the best of our knowledge, this is the first density functional theory (DFT)-based quantification of such a transition for undoped c-ZrO$_2$. Furthermore, we conduct a high-resolution pressure-dependent study (1 GPa increments) covering the range of 1–24 GPa, with particular attention to the less-explored low-pressure regime. This approach enables the detection of subtle anomalies in the elastic and electronic properties that are typically overlooked in studies with coarser pressure increments. Combined with the accurate reproduction of the experimental band gap (~5.8 eV), these results demonstrate the robustness of our computational framework and offer new insights into the intrinsic mechanical and electronic response of c-ZrO$_2$ under

compression. This work thus advances the understanding of the material's behavior in technologically relevant pressure regimes and complements existing experimental studies on the strength and deformation characteristics of zirconia-based ceramics.

The findings of this study have significant implications for the design and application of high-performance ZrO_2-based materials in various fields. These include aerospace components that demand high strength and thermal stability, nuclear materials requiring radiation resistance and mechanical reliability, as well as electronic and optoelectronic devices where bandgap tunability under pressure is a desirable feature. Thus, the present work not only deepens our fundamental understanding of pressure-induced effects in cubic ZrO_2 but also broadens its applicability in advanced functional materials.

2. Materials and Methods

The development of functional materials with desired properties requires either enhancing or suppressing certain characteristics of the original material. Achieving such results is impossible without modern experimental and theoretical approaches. Therefore, it is essential to develop computational models that accurately describe the electronic properties of materials and analyze their structural characteristics. This allows for the precise control and tuning of functional material properties.

One such material, cubic ZrO_2 (c-ZrO_2), is a binary inorganic compound composed of oxygen and zirconium. It crystallizes in a face-centered cubic lattice belonging to the Fm3m space group, where oxygen atoms occupy tetrahedral positions. The elementary rhombohedral unit cell has an edge length of 3.61 Å with angles $\alpha = \beta = \gamma = 60°$ and consists of three atoms with the following crystallographic coordinates: Zr (0, 0, 0), O_1 (0.25, 0.25, 0.25), and O_2 (0.75, 0.75, 0.75). The Zr–O bond lengths are equal, measuring 2.21 Å. The calculated lattice parameter is a = 5.10 Å [33], while the experimental bandgap is reported as 6.1 eV [34]. This lattice parameter was used as the initial value for structural optimization.

In this study, we employed density functional theory (DFT) as implemented in the CRYSTAL23 code [35], which utilizes Kohn–Sham Hamiltonians. DFT calculations serve as a powerful research tool in the design and optimization of new materials. This work presents a comparative study of the structural, electronic, and elastic properties of ZrO_2, using various functionals, including GGA-based PBE [36], PBEsol [37], HSE06 [36], B3LYP [38], B3PW [39], PWGGA [40], and Meta-GGA (SCAN) [41]. All calculations were performed on a Lenovo ThinkStation P620 workstation equipped with an AMD Ryzen™ Threadripper™ PRO 5995WX processor (Manufactured by Lenovo, China, purchased from Server IT LLP, which ordered through the distribution company Lenovo Kazakhstan).

To accurately describe the structural and electronic properties of c-ZrO_2 under hydrostatic pressure, we performed full structural relaxation, optimizing both atomic positions and lattice parameters. The full geometric optimization approach ensured precise lattice configurations. The convergence criteria were set as follows: an energy threshold of 10^{-6} eV, a gradient threshold of $4.5 \cdot 10^{-4}$ eV/Å, and a maximum atomic displacement of $1.8 \cdot 10^{-3}$ Å. The final optimized lattice parameters were a = b = c = 10.2589 Å, $\alpha = \beta = \gamma = 90°$. These optimized parameters serve as a solid foundation for further investigations into the mechanical and electronic properties of c-ZrO_2. To ensure reproducibility and transparency, we provide the original optimization files.

All quantum-chemical calculations were performed using the CRYSTAL23 software package (CRYSTAL23 for Unix/Linux, version v1.0.1; license purchased on 20 December 2023 with an unlimited term of use) and the hybrid density functional method B3LYP, which is widely used in computational materials science [42–51]. Hybrid functionals represent an approximate method for calculating system energy by combining Hartree–Fock exchange energy with exchange–correlation energy derived from density functional approaches. This

hybrid methodology improves the accuracy of parameters that standard DFT functionals often struggle to describe accurately.

In this case, the exchange energy is expressed through Kohn–Sham orbitals rather than electron density, which is why such functionals are referred to as implicit. The application of solutions obtained using the Hartree–Fock method improves the accuracy of calculated parameters that are poorly described by ab initio functionals. Typically, such functionals are constructed as a linear combination of the exchange functional and a set of exchange–correlation functionals operating on electron density. The most-used functional of this type is B3LYP (the three-parameter Becke, Lee–Yang–Parr functional). It is defined by the following expression [52,53]:

$$E_{XC}^{B3LYP} = E_{XC}^{LDA} + a\left(E_X^{HF} - E_X^{LDA}\right) + b\left(E_X^{GGA} - E_X^{LDA}\right) + c\left(E_C^{GGA} - E_C^{LDA}\right) \quad (1)$$

where $a = 0.2$, $b = 0.72$, $c = 0.81$, B3—Becke functional, and LYP—Lee–Yang–Parr correlation functional.

In further calculations, the second-order elastic constants and bulk moduli for polycrystalline samples with optimized geometry [54] were obtained using an automated procedure in CRYSTAL.

The elastic properties of the material, such as the bulk modulus (B), shear modulus (G), Young's modulus (Y), their ratio (B/G), and Poisson's ratio (ν), can be estimated using the Voigt–Reuss–Hill (VRH) approximations. The universal elastic anisotropy index (AU) [53], a semi-empirical formula for assessing mechanical hardness (Hv) [54], and the intrinsic resistance to deformation were also considered. The formulas for these parameters are presented in the literature [54–57].

To study the structural properties of c-ZrO$_2$, a supercell consisting of 96 atoms was used.

3. Results

3.1. Structure of C-ZrO$_2$

Lattice parameter optimization was performed, and the volume, density, and valence bond lengths between atoms in the unit cell were determined. Based on the results obtained from the geometric optimization calculations, a $2 \times 2 \times 2$ supercell was created for the c-ZrO$_2$ structure, consisting of 96 atoms, i.e., 32 Zr atoms and 64 O atoms.

The structure of cubic zirconium dioxide is shown in Figure 1. It was observed that the deviation of the lattice parameters is less than 2% from the reference value of 5.1 Å, depending on the functional used (Table 1). The obtained results were compared with known experimental and theoretical studies [33,58–64].
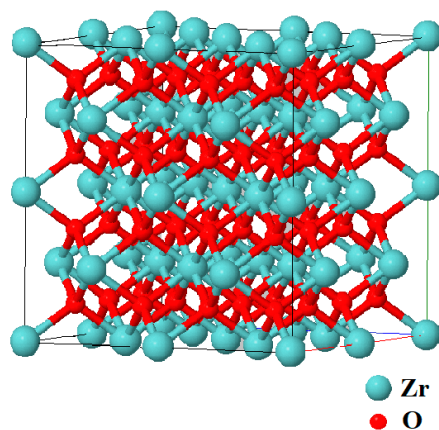

Figure 1. Structure of c-ZrO$_2$.

Table 1. Supercell lattice parameters of c-ZrO$_2$.

Parameters	Functional								
c-ZrO$_2$	**B3LYP**	**B3PW**	**PBE**	**PBE SOL**	**LDA**	**HSE06**	**SCAN**	**Others**	**Experiment**
a = b = c	5.107	5.075	5.104	5.056	5.020	5.067	5.076	5.11 [59] 3.58 [33]	5.11 [60] 3.6012 [61]
V, Å^3	33.31	32.68	33.24	32.32	31.63	32.53	32.69	32.5850 [62]	32.723 [61]
ρ, g/cm^3	6.075	6.192	6.088	6.263	6.398	6.220	6.190	6.081 [63]	6.151 [63]

After optimization, the smallest density error was observed with the PBE functional (6.088 g/cm^3), with an absolute deviation of 0.007. The minimum error in the Zr–O valence bond length was –0.02 Å, which was calculated using the B3PW (2.22 Å) and SCAN (2.2 Å) functionals.

Thus, the geometric structure calculations demonstrated that the results obtained using the DFT method differ only slightly from experimental data [52].

3.2. Band Structure of C-ZrO$_2$

DFT calculations were used to determine the bandgap width corresponding to the equilibrium lattice constant, as well as the electronic structure and density of states (DOS). The calculated bandgap values obtained within the DFT framework using exchange–correlation potentials from the LDA and GGA approximations were compared with experimental and computational data from other authors [36,53,65].

The bandgap width of c-ZrO$_2$ was found to have the following values depending on the standard hybrid functionals used (Table 2). According to our calculations, the most accurate functionals were the three-parameter Becke functional combined with nonlocal correlation PWGGA (B3PW) and the three-parameter Becke functional combined with nonlocal correlation LYP (B3LYP) [52]. The bandgap values obtained using B3LYP (5.17 eV), B3PW (5.2 eV), and HSE06 (5.0 eV) functionals were found to be the closest to the experimental value [50].

Table 2. Band gap of c-ZrO$_2$.

Parameters	Functionals							
c-ZrO$_2$	B3LYP	B3PW	PBE	PBEsol	LDA	HSE06	SCAN	PWGGA
E$_g$, eV (this work)	5.1722	5.2065	3.3195	3.3530	3.3953	5.0088	3.9392	3.2911
Experimental [34]	6.10							
LDA [66]	3.349							
GGA [67]	3.329							

In quantum physics, the energy band parameter is used to describe electronic states, characterizing the distribution of allowed electron energy levels within a crystal. Figure 2 presents the calculated band structure of c-ZrO$_2$ within the first Brillouin zone, indicating high-symmetry points (Γ, L, W, X, Γ) and directions. Due to the symmetry of the Brillouin zone, an energy bandgap is formed, with a width of 5.17 eV for c-ZrO$_2$. This confirms that c-ZrO$_2$ is a dielectric with a direct bandgap along the same symmetry point (Γ-Γ).
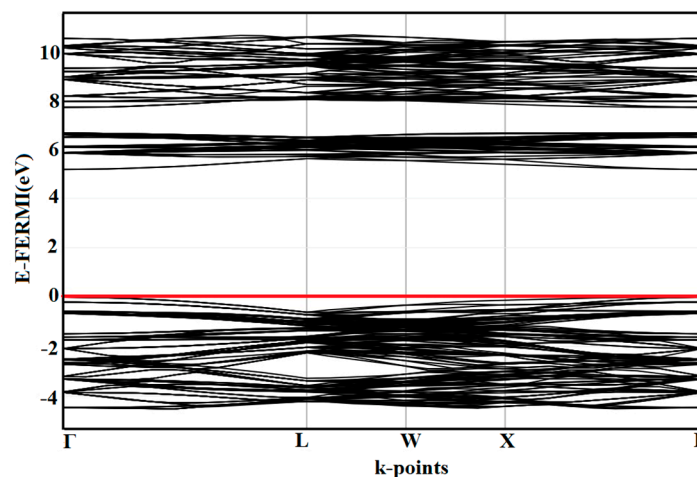
Figure 2. Band structure of c $-ZrO_2$. Redline is Fermi level.

It is well known that the density of states in an energy band corresponds to the number of allowed electron states per energy interval. Figure 3 shows the total electronic density of states for ZrO_2, where the dashed line represents the Fermi level.
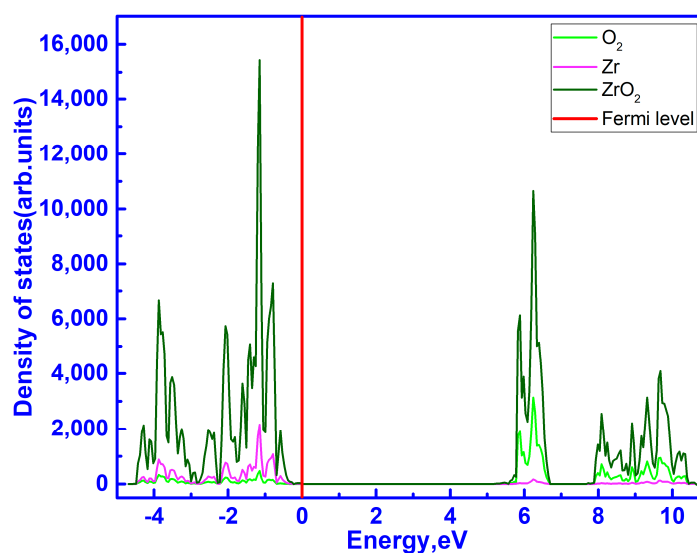

Figure 3. Total and partial density of electronic states ZrO_2.

The upper part of the valence band is predominantly formed by the 2p electrons of oxygen atoms. The 2p electrons of oxygen correspond to the energy range of 0 to –5 eV. In the energy range of 0 to –5 eV in the valence band of zirconium atoms, the partial density of electronic states, which is partially associated with 4d electrons, is significantly lower than that of oxygen atoms (see Figure 3).

The conduction band of c-ZrO_2 is primarily formed by the electronic states of zirconium atoms, with only a minor contribution from the oxygen atoms. From the partial density of states of zirconium atoms, in the energy range of 5.6 to 11 eV, the density of states is associated with unoccupied 4d orbitals of zirconium.

The bandgap width calculated using the B3LYP functional is 5.17 eV for both the primitive cell and the supercell. These results are in good agreement with the findings of other authors [1] on the electronic structure and elastic properties of ZrO_2.

3.3. Elastic Properties of C-ZrO$_2$

Elastic constants provide essential information about the mechanical properties of materials and their structural stability. These properties play a key role in assessing the strength of a material and determining its behavior under applied pressure [66].

Cubic symmetry is characterized by three independent elastic stiffness constants (ESC), namely C_{11}, C_{12}, and C_{44}. According to Hooke's law, at sufficiently small stresses, the deformation is proportional to the applied stress magnitude [56,57,67]:

$$\sigma_i = C_{ij}\varepsilon_j \tag{2}$$

where i, j = 1,2,3....6.

C_{ij} These constants represent elastic stiffness coefficients, where σ_i denotes the applied stress and ε_j corresponds to the resulting strain.

Our calculated values of the elastic constants, bulk modulus, Young's modulus, and shear modulus for c-ZrO$_2$ confirm its mechanical stability under hydrostatic pressure ranging from 0 to 80 GPa. The obtained values at zero pressure are in good agreement with results derived from first-principles calculations [59,66–68].

The relationship $C_{11} > C_{12} > C_{44}$ indicates that c-ZrO$_2$ exhibits the highest resistance to linear compression under hydrostatic pressure. Additionally, C_{44} and G define the intrinsic hardness of the structure under pressure. Both parameters show a consistent trend over the 0–80 GPa pressure range, as illustrated in Figure 4a,b. The increase in G and C_{44} values suggests enhanced hardness and resistance to shear deformation under pressure.
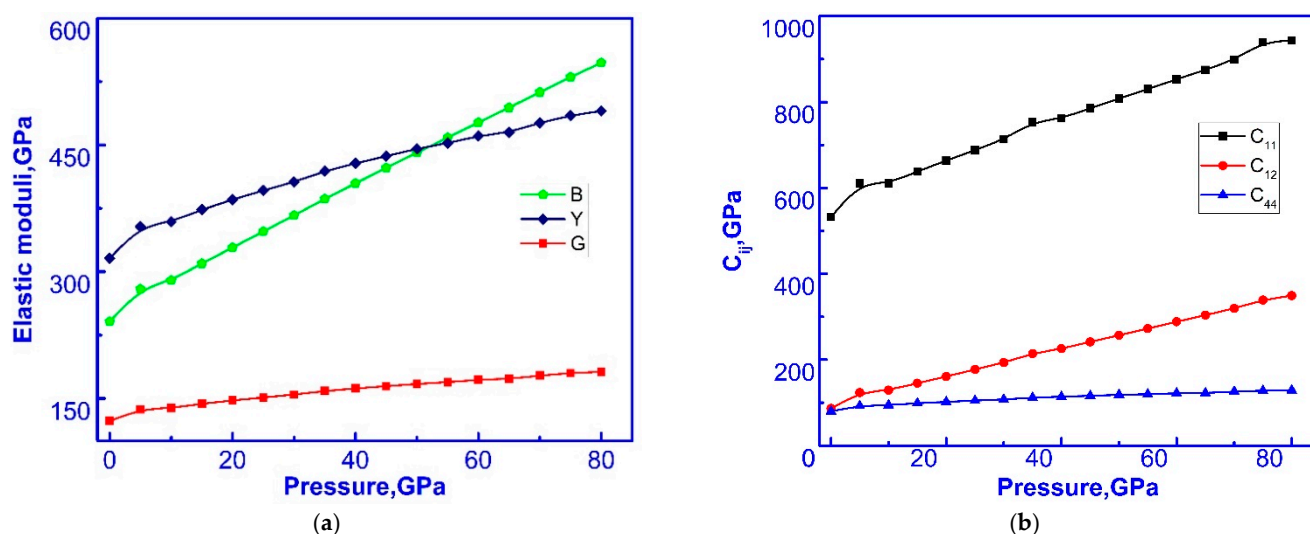

Figure 4. (**a**) Dependence of the bulk modulus, Young's modulus, and compression modulus on the applied hydrostatic pressure. (**b**) Dependence of the elastic constants on the applied pressure.

Furthermore, as shown in Figure 4b, C_{11} and C_{12} increase linearly with pressure compared to C_{44}, indicating their greater sensitivity to high-pressure conditions. Figure 4a demonstrates that B exhibits a linear dependence on applied pressure, increasing from 241.01 GPa at 0 GPa to 547.36 GPa at 80 GPa, confirming its greater hardness and ability to withstand volumetric deformation and failure under high pressure.

Young's modulus (Y) characterizes the stiffness of the material and the ratio of tensile stress to strain under pressure [23]. Figure 4a illustrates that Y increases from 315.91 GPa at 0 GPa to 490.23 GPa at 80 GPa, indicating higher stiffness and enhanced resistance to tensile deformation at elevated pressures.

The calculated Cauchy constants are positive and smoothly increase within the pressure range from 6.5 GPa (at 0 GPa) to 221 GPa (at 80 GPa) (Figure 5a). The ductility of c-ZrO$_2$ is confirmed by the calculated Cauchy difference (C$_{12}$–C$_{44}$) [69,70]. Positive values indicate plasticity, while negative values suggest brittle behavior.
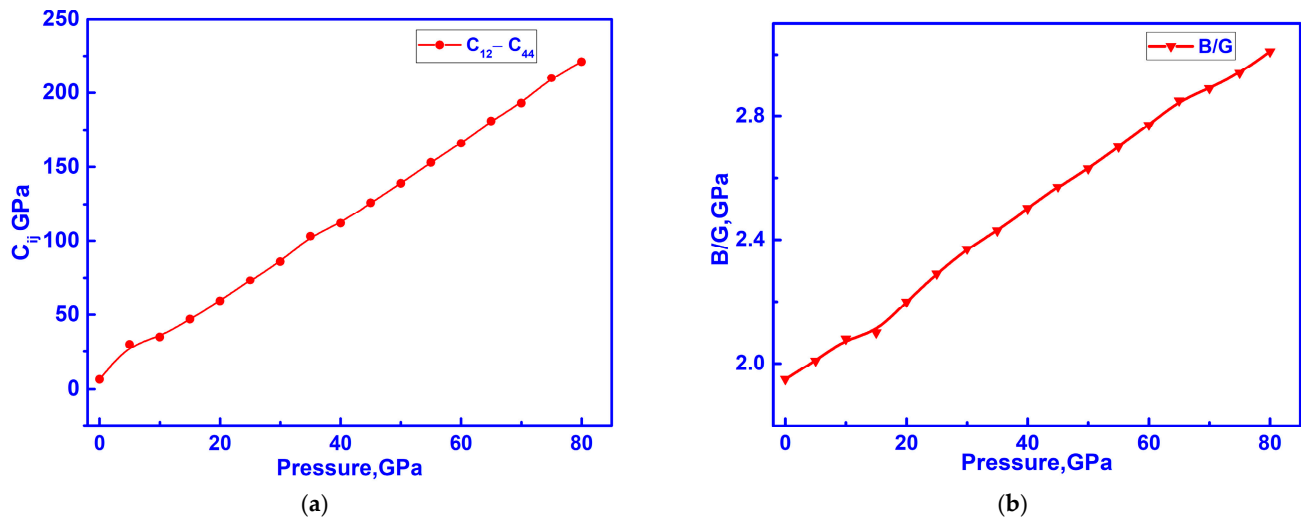

Figure 5. (**a**) Cauchy constants. (**b**) Pugh's criterion.

As shown in Figure 5b, the B/G ratio increases from 1.95 (at 0 GPa) to 3.01 (at 80 GPa), confirming the plasticity of c-ZrO$_2$ according to Pugh's criterion [68]. If a material has B/G < 1.75, it behaves as a brittle material, whereas B/G > 1.75 corresponds to plastic materials.

Poisson's ratio (ν) is 0.282 at 0 GPa and increases to 0.351 at 80 GPa (Figure 6a), further supporting the plasticity of the crystalline structure [69]. Poisson's ratio values of 0.25 and higher indicate an ionic character of bonding between atoms [70]. Our calculations suggest a significant ionic contribution to the intra-atomic bonding of c-ZrO$_2$ up to 80 GPa.
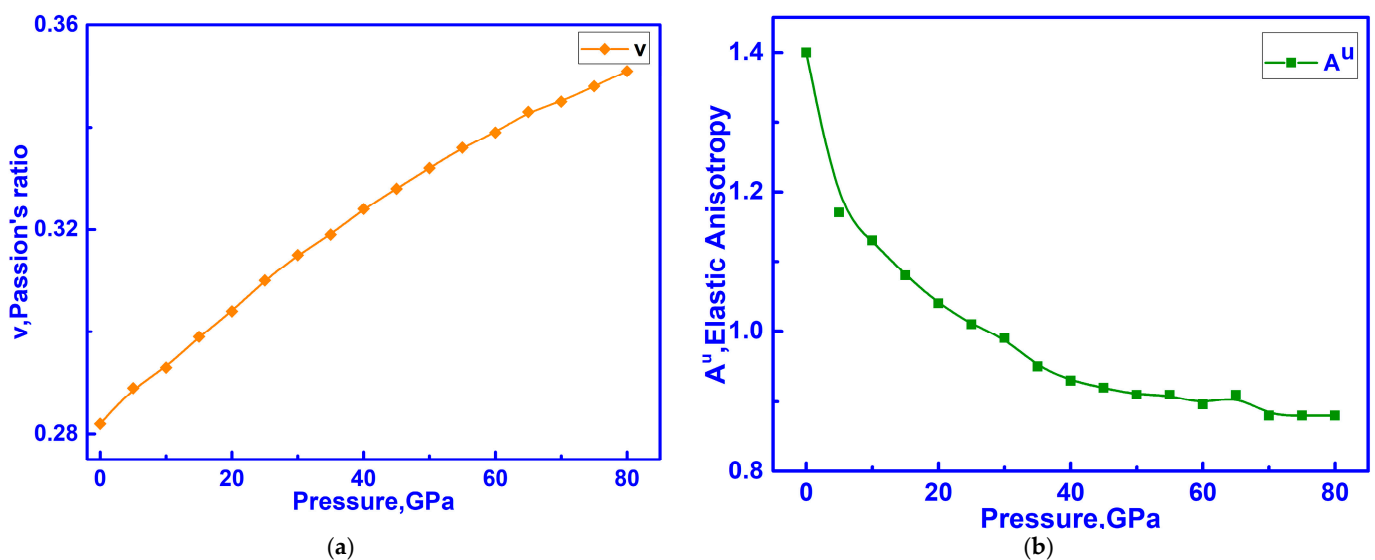

Figure 6. (**a**) Poisson's ratio. (**b**) Anisotropy.

Our calculations showed that the anisotropy index (AU) at zero pressure is 1.4, which is 0.8 lower than the experimental value of 2.21 [71]. A high AU value can lead to reduced elasticity and an increased number of microcracks and microdefects in the material [72].

As pressure increases, the anisotropy of c-ZrO$_2$ decreases from 1.4 to 0.88 at 80 GPa, as shown in Figure 6b. This suggests that the elastic behavior of c-ZrO$_2$ at high pressure implies greater resilience and fewer structural defects and cracks.

Mechanical hardness plays a crucial role among elastic parameters when evaluating the intrinsic strength of a material. Materials are typically classified into three categories: hard, superhard, and ultrahard, with hardness values exceeding 10 GPa, 40 GPa, and 90 GPa, respectively [55].

To demonstrate the effect of pressure on the hardness of cubic ZrO$_2$, we present the calculated Hv values in Figure 6b.

For c-ZrO$_2$, the Hv graph (Figure 7a) shows irregular variations under high pressure. The initial hardness is 13 GPa at zero pressure, with a maximum hardness observed in the range of 5 to 10 GPa. After this, Hv decreases to 9.95 GPa at 40 GPa. The intrinsic hardness of c-ZrO$_2$ decreases from 13 GPa (0 GPa) to 10.3 GPa (80 GPa) under high pressure, classifying c-ZrO$_2$ as a hard material under compression. This indicates that c-ZrO$_2$ exhibits high resistance to compression under pressure.
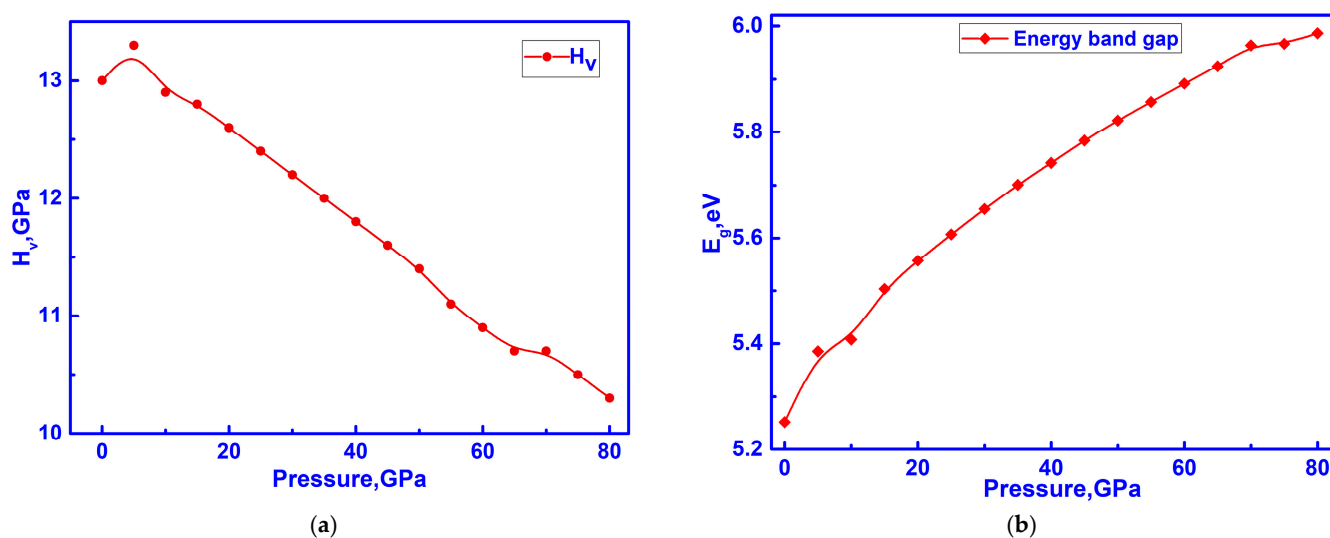

Figure 7. (**a**) Hardness; (**b**) dependence of the bandgap width on hydrostatic pressure.

The calculated bandgap width at zero pressure is in good agreement with the experimental value of 6.1 eV [51].

Contrary to expectations, crystal compression does not significantly increase electronic excitations, as shown in Figure 7b. The bandgap width of c-ZrO$_2$ increases with pressure, from 5.17 eV (0 GPa) to 5.98 eV (80 GPa), confirming its wide bandgap (WBG) behavior under high pressure. These results are in good agreement with experimental data [62]. Figure 8 illustrates that c-ZrO$_2$ compresses under applied pressure. The lattice parameter (a) decreases from 5.129 Å (0 GPa) to 4.787 Å (80 GPa) proportionally to the increase in pressure.

The values obtained at zero pressure align well with the results reported by Zhang et al. [67] and are significantly lower than the theoretical predictions by Muhammad et al. [70]. However, the experimental data from Kandil et al. [71], except for Poisson's ratio, show significant discrepancies compared to our results.

A comprehensive analysis indicates that c-ZrO$_2$ becomes more resistant to compression under high pressures. The improvements in elasticity and hardness under pressure suggest their potential for applications in high-pressure environments.

These findings provide valuable insights into the mechanical behavior of c-ZrO$_2$, which may be crucial for various engineering and materials science applications.
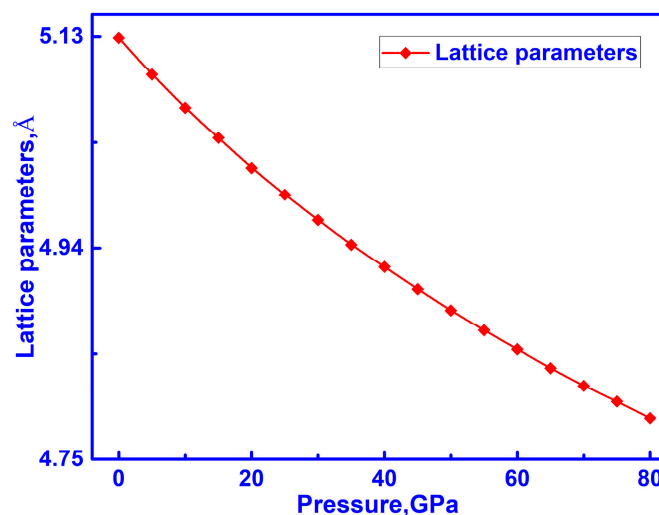
Figure 8. Dependence of lattice parameters on hydrostatic pressure.

3.4. Hidden Anomalies in the Elastic and Electronic Properties of C-ZrO$_2$ Under Low Pressure

During electronic and elastic structure calculations of cubic zirconia (c-ZrO$_2$) in the pressure range of 1–24 GPa with a step of 1 GPa, a set of pressure-dependent physical parameters was obtained, allowing a comprehensive assessment of the material's behavior under external compression. The calculations showed that the lattice parameter (Figure 9a) decreases linearly with increasing pressure, indicating the uniform compression of the crystal structure without signs of a phase transition. The elastic constants C$_{11}$, C$_{12}$, and C$_{44}$ (Figure 9b), as well as the Young's modulus Y, shear modulus G, and bulk modulus B (Figure 10a), also exhibit a monotonic increase, confirming the mechanical stability of the structure throughout the studied range. Moreover, the difference C$_{12}$−C$_{44}$ (Figure 10b) increases linearly, indicating a steady rise in stiffness against directional deformation.
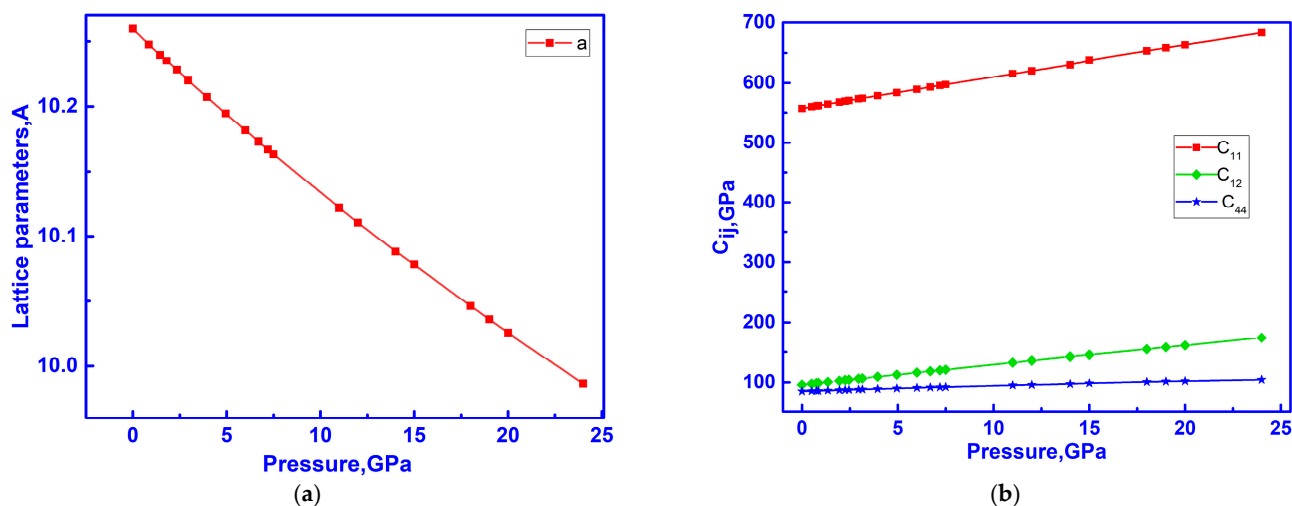

(a)

(b)

Figure 9. (**a**) Dependence of lattice parameters and (**b**) elastic constants on applied pressure.

The Poisson's ratio (Figure 11a) also increases with pressure, but a slight deviation from the smooth trend is observed in the 12–14 GPa range. Similar features are found in the B/G ratio (Figure 11b) and the universal elastic anisotropy A^U (Figure 12a), where subtle bends in the curves are also evident within this pressure interval. These deviations may be interpreted as signs of hidden structural or electronic rearrangements. The most pronounced anomaly appears in the bandgap plot E$_g$ (Figure 12b), where a sharp increase of approximately 0.08 eV is observed between 12 and 14 GPa—clearly deviating from the

otherwise gradual trend. This may indicate a reconstruction of the band structure associated with enhanced overlap between Zr 4d and O 2p orbitals, a redistribution of the electronic density of states, and a possible transition from an indirect to a direct bandgap character.
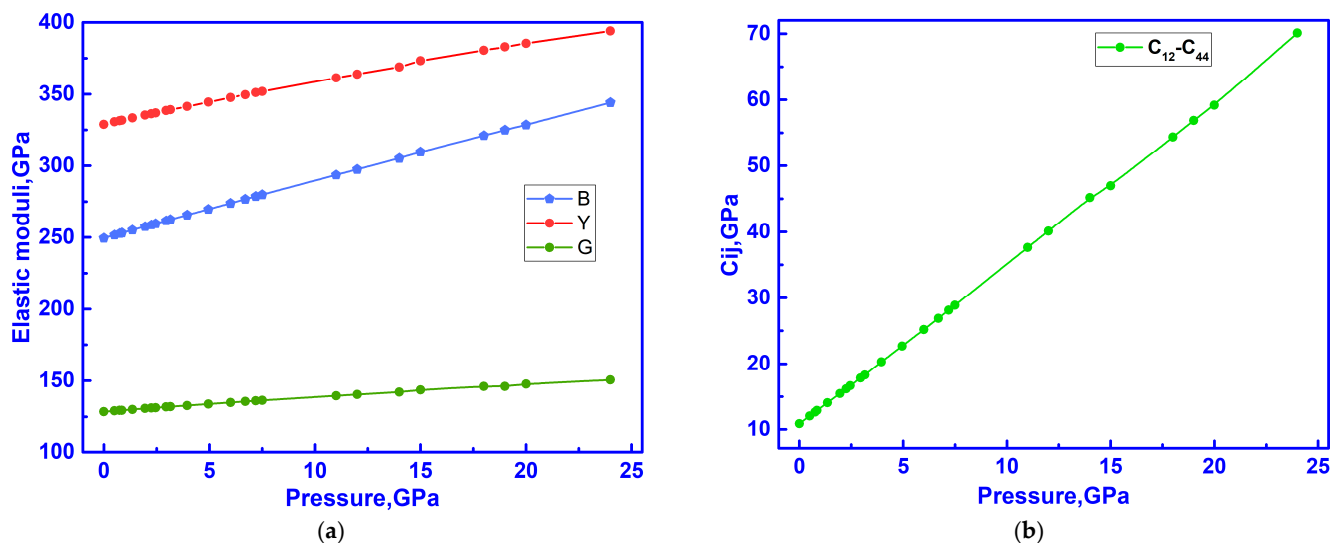

Figure 10. (**a**) Dependence of the bulk modulus, Young's modulus, and compression modulus on the applied hydrostatic pressure. (**b**) Cauchy constants.
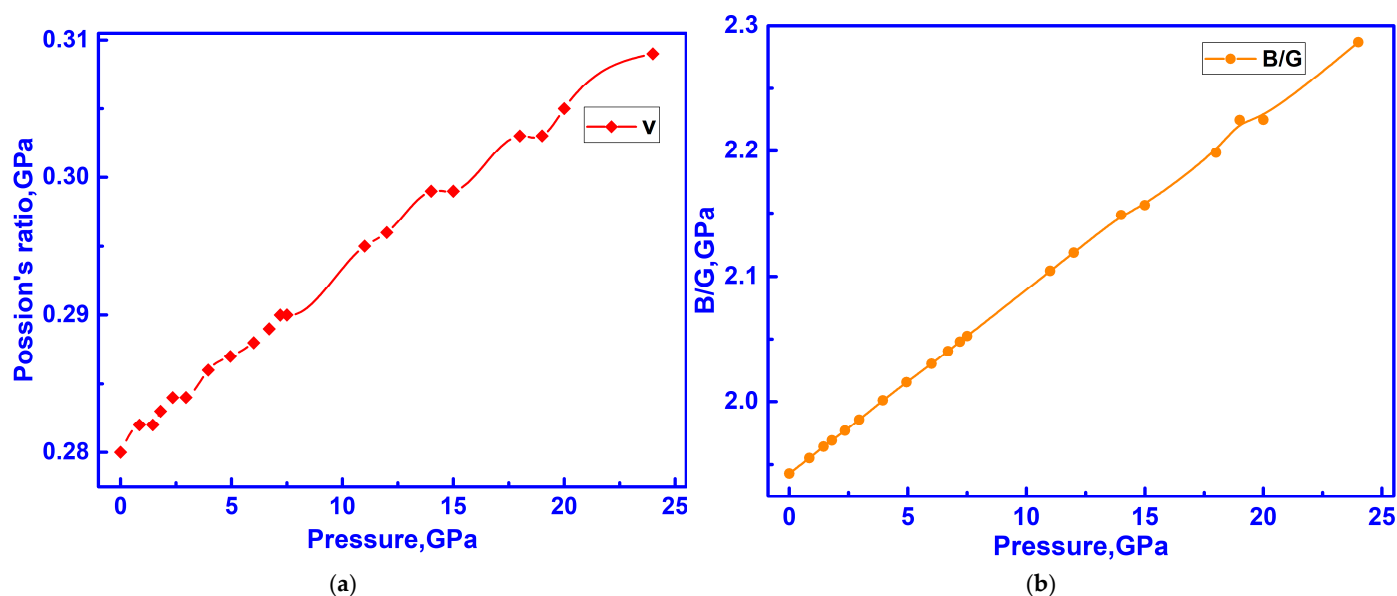

Figure 11. (**a**) Poisson's ratio; (**b**) Pugh's criterion.

Further evidence of these deviations is supported by the non-linearity observed in the stress–strain diagram at stress levels of 2400–2600 MPa (Figure 13), which, according to the literature [73–75], may be attributed to local changes in electronic density, the accumulation of internal defects, and stress redistribution while maintaining the overall cubic symmetry of the crystal.

Thus, despite the apparent linearity of the main elastic parameters, more detailed analysis revealed subtle signs of electronic instability and potential structural rearrangements not previously reported in DFT studies of c-ZrO_2.
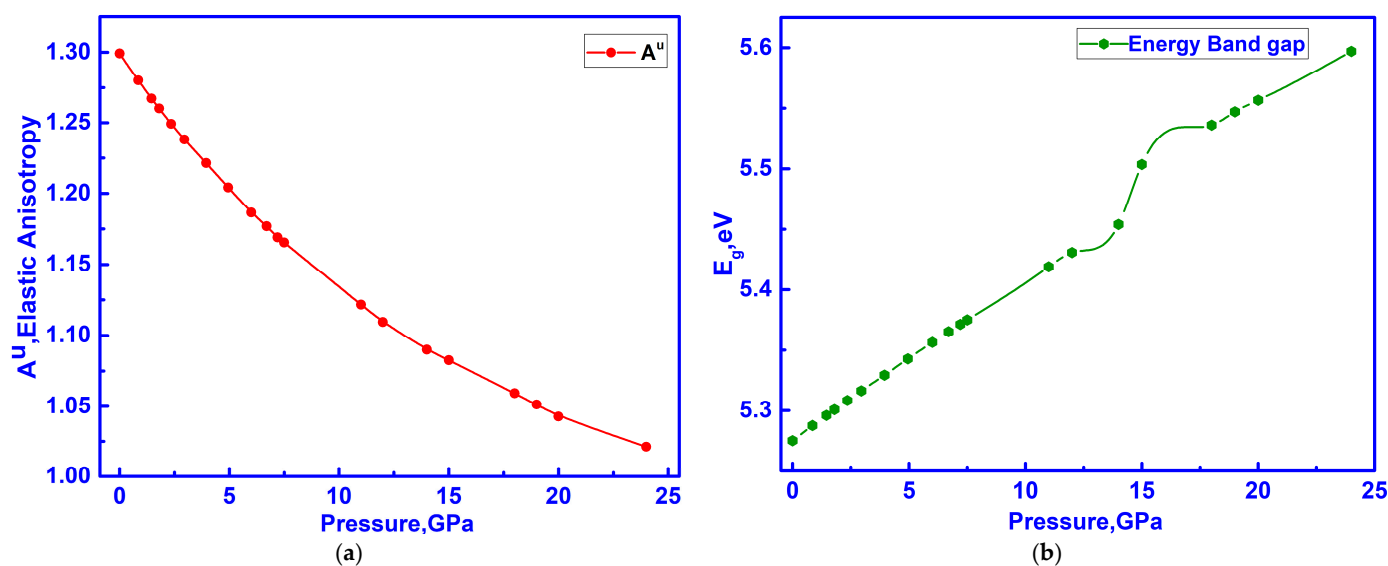
Figure 12. (**a**) Anisotropy. (**b**) Dependence of the bandgap width on hydrostatic pressure.
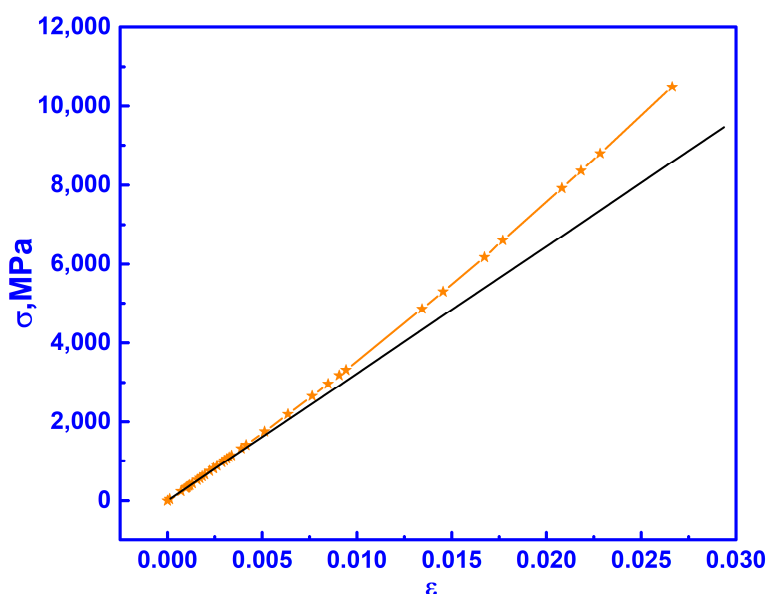

Figure 13. Stress–strain dependence for cubic ZrO_2 under hydrostatic pressure.

4. Discussion and Conclusions

The study of c-ZrO_2 using DFT provided detailed insights into its structural, electronic, and elastic properties. Lattice parameter optimization revealed that the lattice constant of c-ZrO_2 is 5.107 Å, and the Zr–O bond length is 2.21 Å, demonstrating good agreement with known experimental values. This confirms the effectiveness of the B3LYP functional in accurately describing the structural properties of c-ZrO_2.

A comprehensive DFT-based analysis of cubic zirconium dioxide (c-ZrO_2) was conducted to evaluate its structural, electronic, and elastic properties under hydrostatic pressure up to 80 GPa. Bandgap calculations showed that the hybrid functionals B3LYP and B3PW yielded values of 5.17 eV and 5.2 eV, respectively, closely matching the experimental value of 6.1 eV and confirming the accuracy of the chosen computational methods. Elastic property analysis indicated significant mechanical stability, with a bulk modulus (B) of 241 GPa, Young's modulus (Y) of 315.91 GPa, and Poisson's ratio (ν) of 0.282, suggesting good elasticity. The calculated hardness (Hv) of 13 GPa classifies c-ZrO_2 as a hard material, and

the consistent increase in elastic constants under pressure confirms its enhanced stiffness and applicability under extreme mechanical loads.

Importantly, special attention was given to the low-pressure range (1–24 GPa) with high-resolution analysis (1 GPa step), allowing the detection of fine irregularities that are often missed in studies using larger pressure intervals. For the first time, a noticeable change in the bandgap behavior was observed around 12–14 GPa—a sharp increase of approximately 0.08 eV—suggesting a pressure-driven rearrangement of the electronic structure without a phase transition. This effect was accompanied by small shifts in Poisson's ratio, the B/G ratio, and the elastic anisotropy factor A^U, indicating minor changes in interatomic bonding. Furthermore, stress–strain analysis revealed a deviation from linearity in the stress tensor at ~2.4–2.6 GPa, which can be interpreted as the beginning of non-linear mechanical behavior or a theoretical yield point. These findings provide a new understanding of how the electronic and elastic properties of undoped c-ZrO_2 respond to pressure and reveal features not previously reported in the stable cubic phase.

Overall, this study not only deepens the fundamental understanding of pressure effects on c-ZrO_2 but also expands its potential for practical use in advanced functional materials. The results confirm its suitability for applications in electrochemical devices, oxygen sensors, high-strength ceramics, and components for nuclear and aerospace technologies. Future research may focus on the influence of various dopants and defect structures on the material's electronic and mechanical behavior, further broadening its application scope.

In addition, considering recent DFT-based investigations [76] on toxic gas adsorption over oxide surfaces [77–81], the mechanical robustness of c-ZrO_2 demonstrated in this study may also support its role as a stable platform for gas sensing and environmental remediation technologies. The combination of structural integrity under pressure and potential surface reactivity highlights its multifunctionality for emerging applications.

Institutional Review Board Statement: Not applicable.

Informed Consent Statement: Not applicable.

Data Availability Statement: The original contributions presented in this study are included in the article. Further inquiries can be directed to the corresponding author.

Conflicts of Interest: This work has been carried out within the framework of the EUROfusion Consortium, funded by the European Union via the Euratom Research and Training Programme (Grant Agreement No 101052200—EUROfusion). The views and opinions expressed are however those of the author(s) only and do not necessarily reflect those of the European Union or the European Commission. Neither the European Union nor the European Commission can be held responsible for them.

References

1. Muñoz, M.C.; Gallego, S.; Beltrán, J.I.; Cerdá, J. Adhesion at metal–ZrO$_2$ interfaces. *Surf. Sci. Rep.* **2006**, *61*, 303–344. [CrossRef]
2. Kisi, E.H.; Howard, C.J. Crystal structures of zirconia phases and their inter-relation. *Key Eng. Mater.* **1998**, *153*, 1–36. [CrossRef]
3. Luthardt, R.G.; Sandkuhl, O.; Herold, V. Reliability and properties of ground Y-TZP-zirconia ceramics. *J. Dent. Res.* **2002**, *81*, 487–491. [CrossRef]
4. Jin, L.; Yu, Q.; Rauf, A.; Zhou, C. Elastic, electronic and thermal properties of YSZ from first principles. *Solid State Sci.* **2012**, *14*, 106. [CrossRef]
5. Garzon, F.H.; Mukundan, R.; Lujan, R.; Brosha, E.L. Solid state ionic devices for combustion gas sensing. *Solid State Ion.* **2004**, *175*, 487. [CrossRef]
6. Fleischhauer, F.; Bermejo, R.; Danzer, R.; Mai, A.; Graule, T.; Kuebler, J. High temperature mechanical properties of zirconia tapes used for electrolyte supported solid oxide fuel cells. *J. Power Sources* **2015**, *273*, 237. [CrossRef]
7. Messaddeq, S.H.; Pulcinelli, S.H.; Santilli, C.V.; Guastaldi, A.C.; Messaddeq, Y. Microstructure and corrosion resistance of inorganic–organic (ZrO2–PMMA) hybrid coating on stainless steel. *J. Non-Cryst. Solids* **1999**, *247*, 164. [CrossRef]
8. Ananchenko, D.V.; Nikiforov, S.V.; Sobyanin, K.V.; Konev, S.F.; Dauletbekova, A.K.; Akhmetova-Abdik, G.; Akilbekov, A.T.; Popov, A.I. Paramagnetic Defects and Thermoluminescence in Irradiated Nanostructured Monoclinic Zirconium Dioxide. *Materials* **2022**, *15*, 8624. [CrossRef]
9. Ali, I.; Imanova, G.T.; Garibov, A.A.; Agayev, T.N.; Jabarov, S.H.; Almalki, A.S.; Alsubaie, A. Gamma rays mediated water splitting on nano-ZrO2 surface: Kinetics of molecular hydrogen formation. *Radiat. Phys. Chem.* **2021**, *183*, 109431. [CrossRef]
10. Qi, S.; Porotnikova, N.M.; Ananyev, M.V.; Kuzmin, A.V.; Eremin, V.A.; Pankratov, A.A.; Molchanova, N.G.; Reznitskikh, O.G.; Farlenkov, A.S.; Vovkotrub, E.G.; et al. High-temperature glassy-ceramic sealants SiO$_2$-Al$_2$O$_3$-BaO-MgO and SiO$_2$-Al$_2$O$_3$-ZrO$_2$-CaO-Na$_2$O for solid oxide electrochemical devices. *Trans. Nonferr. Met. Soc. China* **2016**, *26*, 2916–2924. [CrossRef]
11. Farlenkov, A.S.; Ananyev, M.V.; Eremin, V.A.; Porotnikova, N.M.; Kurumchin, E.K.; Melekh, B.T. Oxygen isotope exchange in doped calcium and barium zirconates. *Solid State Ion.* **2016**, *290*, 108–115. [CrossRef]
12. Dauletbekova, A.; Zvonarev, S.; Nikiforov, S.; Akilbekov, A.; Shtang, T.; Karavannova, N.; Akylbekova, A.; Ishchenko, A.; Akhmetova-Abdik, G.; Baymukhanov, Z.; et al. Luminescence Properties of ZrO$_2$: Ti Ceramics Irradiated with Electrons and High-Energy Xe Ions. *Materials* **2024**, *17*, 1307. [CrossRef]
13. Kozlovskiy, A.L.; Konuhova, M.; Borgekov, D.B. Study of irradiation temperature effect on radiation-induced polymorphic transformation mechanisms in ZrO2 ceramics. *Opt. Mater.* **2024**, *156*, 115994. [CrossRef]
14. Imanova, G.T.; Agayev, T.N.; Jabarov, S.H. Investigation of structural and optical properties of zirconia dioxide nanoparticles by radiation and thermal methods. *Mod. Phys. Lett. B* **2021**, *35*, 2150050. [CrossRef]
15. Kozlovskiy, A.L.; Konuhova, M.; Shlimas, D.I.; Borgekov, D.B.; Zdorovets, M.V.; Shakirziyanov, R.I.; Popov, A.I. Study of the Effect of Nanostructured Grains on the Radiation Resistance of Zirconium Dioxide Ceramics During Gas Swelling under High-dose Irradiation with Helium Ions. *ES Mater. Manuf.* **2024**, *24*, 1165. [CrossRef]
16. Kadyrzhanov, K.K.; Kozlovskiy, A.A.; Konuhova, M.; Popov, A.I.; Shlimas, D.D.; Borgekov, D.B. Determination of gamma radiation shielding efficiency by radiation-resistant composite ZrO$_2$-Al$_2$O$_3$-TiO$_2$-WO$_3$-Nb$_2$O$_5$ ceramics. *Opt. Mater.* **2024**, *154*, 115752. [CrossRef]
17. Abyshev, B.K.; Giniyatova, S.G.; Kozlovskiy, A.L. Effect of irradiation temperature on the mobility of structural and vacancy defects in the damaged layer of Li$_2$ZrO$_3$ ceramics. *Opt. Mater. X* **2024**, *24*, 100376. [CrossRef]
18. Kozlovskiy, A.L.; Alin, M.; Borgekov, D.B. Study of Polymorphic Transformation Processes and Their Influence in Polycrystalline ZrO$_2$ Ceramics upon Irradiation with Heavy Ions. *Ceramics* **2023**, *6*, 686–706. [CrossRef]
19. Teufer, G. The crystal structure of tetragonal ZrO$_2$. *Acta Crystallogr.* **1962**, *15*, 1187. [CrossRef]
20. Suchanek, W.; Yoshimura, M. Processing and properties of hydroxyapatite-based biomaterials for use as hard tissue replacement implants. *J. Mater. Res.* **1998**, *13*, 94–117. [CrossRef]
21. Harmsworth, P.; Stevens, R. Phase composition and properties of plasma-sprayed zirconia thermal barrier coatings. *J. Mater. Sci.* **1992**, *27*, 611–615. [CrossRef]
22. McCullough, J.T.; Trueblood, K. The crystal structure of baddeleyite (monoclinic ZrO$_2$). *Acta Crystallogr.* **1959**, *12*, 507–511. [CrossRef]
23. Bandura, A.V.; Evarestov, R.A. Ab initio structure modeling of ZrO$_2$ nanosheets and single-wall nanotubes. *Comput. Mater. Sci.* **2012**, *65*, 395–405. [CrossRef]
24. Howard, C.J.; Hill, R.J.; Reichert, B.E. Structures of the polymorphs of the high-temperature superconductor YBa$_2$Cu$_3$O$_{7-x}$. *Acta Crystallogr. B* **1988**, *44*, 116–120. [CrossRef]
25. Garvie, R.C.; Hannink, R.H.; Pascoe, R.T. Ceramic steel? *Nature* **1975**, *258*, 703. [CrossRef]
26. Roth, W.L. *Crystal Structure and Chemical Bonding in Inorganic Chemistry*; Rooymans, C.J., Rabenau, A., Eds.; North-Holland Publishing Company: Amsterdam, The Netherlands, 1975; pp. 85–102.

27. Proffen, T.; Neder, R.B.; Frey, F.; Assmus, W. Defect structure and diffuse scattering of zirconia single crystals doped with 7 mol% CaO. *Acta Crystallogr. B* **1993**, *49*, 599. [CrossRef]

28. Hevorkian, E.; Jozwik, J.; Rucki, M.; Kolodnitskyi, V.; Morozova, O.; Dziedzic, K. Reproducibility of properties of zirconia-based composites. In Proceedings of the 2024 11th International Workshop on Metrology for AeroSpace (MetroAeroSpace), Lublin, Poland, 3–5 June 2024; IEEE: Piscataway, NJ, USA, 2024; pp. 484–489.

29. Sun, N.; Zhu, T.; Zeng, Y.; Wang, Y.; Wang, H.; Li, Y.; Sang, S.; Xie, Z.; Cao, H. Achieving excellent toughness and wear resistance in WC-ZrO$_2$-Al$_2$O$_3$ ceramics by combining laminated structure and two-step oscillatory pressure sintering. *SSRN* **2024**, 5027477. [CrossRef]

30. Wu, H.; Duan, Y.; Liu, K.; Lv, D.; Qin, L.; Shi, L.; Tang, G. First-principles study of phase transition and band structure of ZrO$_2$ under pressure. *J. Alloys Compd.* **2015**, *645*, 352–357. [CrossRef]

31. Eklund, K.; Alajoki, J.; Karttunen, A.J. Elastic properties of binary d-metal oxides studied by hybrid density functional methods. *Cryst. Growth Des.* **2023**, *23*, 3427–3436. [CrossRef]

32. Mirgorodsky, A.P.; Quintard, P.E. Lattice-dynamic treatment of vibrational and elastic properties of cotunnite-type ZrO$_2$ and HfO$_2$: Comparison with ambient pressure polymorphs. *J. Am. Ceram. Soc.* **1999**, *82*, 3121–3124. [CrossRef]

33. Muhammad, I.D.; Awang, M. Modelling the interatomic potential of cubic zirconia. *Appl. Mech. Mater.* **2013**, *446–447*, 151–157. [CrossRef]

34. French, R.H.; Glass, S.J.; Ohuchi, F.S.; Xu, Y.-N.; Ching, W.Y. Experimental and theoretical determination of the electronic structure and optical properties of three phases of ZrO$_2$. *Phys. Rev. B* **1994**, *49*, 5133–5142. [CrossRef]

35. Erba, A.; Desmarais, J.K.; Casassa, S.; Civalleri, B.; Donà, L.; Bush, I.J.; Searle, B.; Maschio, L.; Edith-Daga, L.; Cossard, A.; et al. CRYSTAL23: A program for computational solid-state physics and chemistry. *J. Chem. Theory Comput.* **2023**, *19*, 6891–6932. [CrossRef]

36. Perdew, J.P.; Burke, K.; Ernzerhof, M. Generalized Gradient Approximation Made Simple. *Phys. Rev. Lett.* **1996**, *77*, 3865–3868. [CrossRef]

37. Perdew, J.P.; Ruzsinszky, A.; Csonka, G.I.; Vydrov, O.A.; Scuseria, G.E.; Zhou, X.; Burke, K. Restoring the Density-Gradient Expansion for Exchange in Solids and Surfaces. *Phys. Rev. Lett.* **2008**, *100*, 136406. [CrossRef]

38. Vosko, S.H.; Wilk, L.; Nusair, M. Accurate spin-dependent electron liquid correlation energies for local spin density calculations: A critical analysis. *Can. J. Phys.* **1980**, *58*, 1200. [CrossRef]

39. Ziesche, P.; Eschrig, H. (Eds.) *Electronic Structure of Solids' 91: Proceedings of the 75. WE-Heraeus-Seminar and 21st Annual International Symposium on Electronic Structure of Solids Held in Gaussig (Germany), March 11–15, 1991*; De Gruyter Akademie Forschung: Berlin, Germany, 1991; Volume 17.

40. Perdew, J.P.; Chevary, J.A.; Vosko, S.H.; Jackson, K.A.; Pederson, M.R.; Singh, D.J.; Fiolhais, C. Atoms, molecules, solids, and surfaces: Applications of the generalized gradient approximation for exchange and correlation. *Phys. Rev. B* **1992**, *46*, 6671. [CrossRef]

41. Sun, J.; Ruzsinszky, A.; Perdew, J.P. Strongly constrained and appropriately normed semilocal density functional. *Phys. Rev. Lett.* **2015**, *115*, 036402. [CrossRef] [PubMed]

42. Eglitis, R.I.; Popov, A.I.; Jia, R.; Kruchinin, S.P.; Derkaoui, I.; Kabatas, M.A. B3LYP and B3PW computations of BaSnO$_3$ and BaZrO$_3$ perovskite (001) surfaces. *Low Temp. Phys.* **2024**, *50*, 905–910. [CrossRef]

43. Kaptagay, G.A.; Satanova, B.M.; Abuova, A.U.; Konuhova, M.; Zakiyeva, Z.Y.; Tolegen, U.Z.; Koilyk, N.O.; Abuova, F.U. Effect of rhodium doping for photocatalytic activity of barium titanate. *Opt. Mater. X* **2025**, *25*, 100382. [CrossRef]

44. Rusevich, L.L.; Brik, M.G.; Gryaznov, D.; Srivastava, A.M.; Chervyakov, I.; Zvejnieks, G.; Bocharov, D.; Kotomin, E.A. First-Principles Linear Combination of Atomic Orbitals Calculations of K$_2$SiF$_6$ Crystal: Structural, Electronic, Elastic, Vibrational and Dielectric Properties. *Materials* **2024**, *17*, 4865. [CrossRef] [PubMed]

45. Piasecki, M.; Myronchuk, G.L.; Zamurueva, O.V.; Khyzhun, O.Y.; Parasyuk, O.V.; Fedorchuk, A.O.; Albassam, A.; El-Naggar, A.M.; Kityk, I.V. Huge operation by energy gap of novel narrow band gap Tl$_{1-x}$In$_{1-x}$BxSe$_2$ (B = Si, Ge): DFT, X-ray emission and photoconductivity studies. *Mater. Res. Express* **2016**, *3*, 025902. [CrossRef]

46. Lisovski, O.; Chesnokov, A.; Piskunov, S.; Bocharov, D.; Zhukovskii, Y.F.; Wessel, M.; Spohr, E. Ab initio calculations of doped TiO$_2$ anatase (101) nanotubes for photocatalytical water splitting applications. *Mat. Sci. Semicon. Proc.* **2016**, *42*, 138–141. [CrossRef]

47. Rudysh, M.Y.; Brik, M.G.; Stadnyk, V.Y.; Brezvin, R.S.; Shchepanskyi, P.A.; Fedorchuk, A.; Khyzhun, O.Y.; Kityk, I.V.; Piasecki, M. Ab initio calculations of the electronic structure and specific optical features of β-LiNH$_4$SO$_4$ single crystals. *Phys. B Condens. Matter* **2018**, *528*, 37–46. [CrossRef]

48. Ma, C.G.; Brik, M.G. Hybrid density-functional calculations of structural, elastic and electronic properties for a series of cubic perovskites CsMF$_3$ (M= Ca, Cd, Hg, and Pb). *Comput. Mater. Sci.* **2012**, *58*, 101–112. [CrossRef]

49. Rudysh, M.Y.; Brik, M.G.; Khyzhun, O.Y.; Fedorchuk, A.O.; Kityk, I.V.; Shchepanskyi, P.A.; Stadnyk, V.Y.; Lakshminarayana, G.; Brezvin, R.S.; Bak, Z.; et al. Ionicity and birefringence of α-LiNH$_4$SO$_4$ crystals: Ab initio DFT study, X-ray spectroscopy measurements. *RSC Adv.* **2017**, *7*, 6889–6901. [CrossRef]

50. Buryi, M.; Babin, V.; Děcká, K.; Ridzoňová, K.; Neykova, N.; Hájek, F.; Velkov, Z.; Remeš, Z.; Tomala, R.; Socha, P. Charge trapping and luminescence of the mixed size CsPbBr$_3$ particles grown in one batch. *Opt. Mater.* **2024**, *151*, 115279. [CrossRef]

51. Parasyuk, O.V.; Babizhetskyy, V.S.; Khyzhun, O.Y.; Levytskyy, V.O.; Kityk, I.V.; Myronchuk, G.L.; Tsisar, O.V.; Piskach, L.V.; Jedryka, J.; Maciag, A.; et al. Novel Quaternary TlGaSn$_2$Se$_6$ Single Crystal as Promising Material for Laser Operated Infrared Nonlinear Optical Modulators. *Crystals* **2017**, *7*, 341. [CrossRef]

52. Becke, A.D. Density-functional thermochemistry. *III. The role of exact exchange. J. Chem. Phys.* **1993**, *98*, 5648. [CrossRef]

53. Perger, W.F.; Criswell, C.; Civalleri, B.; Dovesi, R. Ab-initio calculation of elastic constants of crystalline systems with the CRYSTAL code. *Comput. Phys. Commun.* **2009**, *180*, 1753–1759. [CrossRef]

54. Erba, A.; Mahmoud, A.; Orlando, R.; Dovesi, R. Elastic properties of six silicate garnet end-members from accurate ab initio simulations. *Phys. Chem. Miner.* **2014**, *41*, 151–160. [CrossRef]

55. Kishore, N.; Nagarajan, V.; Chandiramouli, R. First-principles studies on mechanical properties and band structures of TMO2 (TM = Zr or Hf) nanostructures under high pressure. *Phys. B Condens. Matter* **2019**, *559*, 1–7. [CrossRef]

56. Terki, R.; Feraoun, H.; Bertrand, G.; Aourag, H. First principles calculations of structural, elastic and electronic properties of XO2 (X=Zr, Hf and Th) in fluorite phase. *Comput. Mater. Sci.* **2005**, *33*, 44–52. [CrossRef]

57. Jamal, M.; Asadabadi, S.J.; Ahmad, I.; Aliabad, H.R. Elastic constants of cubic crystals. *Comput. Mater. Sci.* **2014**, *95*, 592–599. [CrossRef]

58. Yang, J.; Shahid, M.; Wan, C.; Jing, F.; Pan, W. Anisotropy in elasticity, sound velocities and minimum thermal conductivity of zirconia from first-principles calculations. *J. Eur. Ceram. Soc.* **2017**, *37*, 689–695. [CrossRef]

59. Zhang, Y.; Chen, H.-X.; Duan, L.; Fan, J.-B.; Ni, L.; Ji, V. A comparison study of the structural and mechanical properties of cubic, tetragonal, monoclinic, and three orthorhombic phases of ZrO$_2$. *J. Alloy. Compd.* **2018**, *749*, 283–292. [CrossRef]

60. Khitrova, V.I.; Klechkovskaya, V.V. Electron-diffraction investigation of phase transformation and crystal structure of thin layers of cubic zirconium oxide. *Kristallografiya* **1985**, *30*, 126–130.

61. Soo, Y.L.; Chen, P.J.; Huang, S.H.; Shiu, T.J.; Tsai, T.Y.; Chow, Y.H.; Lin, Y.C.; Weng, S.C.; Chang, S.L.; Wang, G.; et al. Local Structures Surrounding Zr in Nanostructurally Stabilized Cubic Zirconia: Structural Origin of Phase Stability. *J. Appl. Phys.* **2008**, *104*, 113535. [CrossRef]

62. Wang, C. Multiscale Modeling and Simulation of Nanocrystalline Zirconium Oxide. Ph.D. Thesis, University of Nebraska, Lincoln, Nebraska, 2009.

63. Chang, Y.; Wang, H.; Zhu, Q.; Luo, P.; Dong, S. Theoretical calculation and analysis of ZrO$_2$ spherical nanometer powders. *J. Adv. Ceram.* **2013**, *2*, 21–25. [CrossRef]

64. Suciu, C.; Gagea, L.; Hoffmann, A.C.; Mocean, M. Sol-gel production of zirconia nanoparticles with a new organic precursor. *Chem. Eng. Sci.* **2006**, *61*, 7831–7835. [CrossRef]

65. Nematov, D.D.; Burhonzoda, A.S.; Kholmurodov, K.T.; Lyubchyk, A.I.; Lyubchyk, S.I. A detailed comparative analysis of the structural stability and electron-phonon properties of ZrO$_2$: Mechanisms of water adsorption on t-ZrO$_2$ (101) and t-YSZ (101) surfaces. *Nanomaterials* **2023**, *13*, 2657. [CrossRef] [PubMed]

66. Erba, A.; Mahmoud, A.; Belmonte, D.; Dovesi, R. High pressure elastic properties of minerals from *ab initio* simulations: The case of pyrope, grossular and andradite silicate garnets. *J. Chem. Phys.* **2014**, *140*, 124703. [CrossRef] [PubMed]

67. Nazir, M.A.; Mahmood, T.; Zafar, A.A.; Akhtar, N.; Hussain, T.; Saeed, M.A.; Aleem, F.-E.; Saeed, A.; Raza, J.; Cao, C. Electronic, optical, and elastic properties of cubic zirconia (c-ZrO$_2$) under pressure: A DFT study. *Phys. B Condens. Matter* **2021**, *604*, 412462. [CrossRef]

68. Pugh, S. XCII. Relations between the elastic moduli and the plastic properties of polycrystalline pure metals. *Lond. Edinb. Dublin Philos. Mag. J. Sci.* **1954**, *45*, 823–843. [CrossRef]

69. Kishore, N.; Nagarajan, V.; Chandiramouli, R. Mechanical properties and band structure of CdSe and CdTe nanostructures at high pressure - a first-principles study. *Process. Appl. Ceram.* **2019**, *13*, 124–131. [CrossRef]

70. Kong, Y.; Duan, Y.; Ma, L.; Li, R. Phase stability, elastic anisotropy and electronic structure of cubic MAl$_2$(M = Mg, Ca, Sr and Ba) Laves phases from first-principles calculations. *Mater. Res. Express* **2016**, *3*, 106505. [CrossRef]

71. Kishore, N.; Nagarajan, V.; Chandiramouli, R. Mechanical and electronic properties under high pressure on ternary AlGaN and InGaN compounds—a first-principles perspective. *Mater. Res. Express* **2018**, *6*, 015052. [CrossRef]

72. Zhao, X.-S.; Shang, S.-L.; Liu, Z.-K.; Shen, J.-Y. Elastic properties of cubic, tetragonal and monoclinic ZrO$_2$ from first-principles calculations. *J. Nucl. Mater.* **2011**, *415*, 13–17. [CrossRef]

73. Morita, K.; Sekino, T.; Niihara, K. Fracture strength and toughness of nanocrystalline cubic zirconia prepared by HIPing. *J. Eur. Ceram. Soc.* **2006**, *26*, 1521–1525. [CrossRef]

74. Promakhov, V.V.; Buyakova, S.P. Structural and mechanical behavior of ultrafine-grained ZrO$_2$-based ceramics under shock-wave loading. *Powder Metall. Struct. Mater.* **2019**, *5*, 23–31.

75. Vasileva, A.M.; Kulkov, S.E. Mechanical and structural properties of ZrO$_2$–MgO composites with different porosity levels. *J. Mech. Behav. Mater.* **2017**, *26*, 121–126.

76. Ullah, Z.; Sattar, F.; Kim, H.J.; Jang, S.; Mary, Y.S.; Zhan, X.; Kwon, H.W. Computational study of toxic gas removal. *J. Mol. Liq.* **2022**, *365*, 120213. [CrossRef]

77. Hichem, N.; Hadjer, Z.; Fateh, S.; Feriel, L.; Wang, Z. The potential exposure and hazards of zirconia nanoparticles: A review. *Ecotoxicol. Environ. Contam.* **2022**, *17*, 1–21. [CrossRef]

78. Lyashenko, E.N.; Uzbekova, L.D.; Polovinkina, V.V.; Dorofeeva, A.K.; Ibragimov, S.-U.S.-U.; Tatamov, A.A.; Avkaeva, A.G.; Mikhailova, A.A.; Tuaeva, I.S.; Esiev, R.K.; et al. Study of the Embryonic Toxicity of TiO_2 and ZrO_2 Nanoparticles. *Micromachines* **2023**, *14*, 363. [CrossRef] [PubMed]

79. Chitoria, A.K.; Mir, A.; Shah, M.A. A review of ZrO_2 nanoparticles applications and recent advancements. *Ceram. Int.* **2023**, *49*, 32343–32358. [CrossRef]

80. Ramanavicius, S.; Jagminas, A.; Ramanavicius, A. Gas sensors based on titanium oxides. *Coatings* **2022**, *12*, 699. [CrossRef]

81. Usseinov, A.B.; Akilbekov, A.T.; Kotomin, E.A.; Karipbayev, Z.T. The first principles calculations of CO_2 adsorption on (1010) ZnO surface. *AIP Conf. Proc.* **2019**, *2174*, 020181.